

# Topochemistry-Driven Synthesis of Transition-Metal Selenides with Weakened Van Der Waals Force to Enable 3D-Printed Na-Ion Hybrid Capacitors

Wei Zong, Hele Guo, Yue Ouyang, Lulu Mo, Chunyang Zhou, Guojie Chao, Johan Hofkens, Yang Xu, Wei Wang, Yue-E Miao, Guanjie He, Ivan P. Parkin, Feili Lai,\* and Tianxi Liu\*

Hybrid capacitors exhibit promise to bridge the gap between rechargeable high-energy density batteries and high-power density supercapacitors. This separation is due to sluggish ion/electron diffusion and inferior structural stability of battery-type materials. Here, a topochemistry-driven method for constructing expanded 2D rhenium selenide intercalated by nitrogen-doped carbon hybrid (E-ReSe<sub>2</sub>@INC) with a strong-coupled interface and weak van der Waals forces, is proposed. X-ray absorption spectroscopy analysis dynamically tracks the transformation from Re–O into Re–C bonds. The bridging bonds act as electron transport channels to enable improved conductivity and accelerated reaction kinetics. The expanded interlayer-spacing of ReSe<sub>2</sub> layer by INC facilitates ion diffusion and ensures structural stability. As expected, the E-ReSe<sub>2</sub>@INC achieves an improved rate capability (252.5 mAh g<sup>-1</sup> at 20 A g<sup>-1</sup>) and long-term cyclability (89.6% over 3500 cycles). Moreover, theoretical simulations reveal the favorable Na<sup>+</sup> storage kinetics can be ascribed to its low bonding energy of –0.06 eV and diffusion barrier of 0.08 eV for sodium ions. Additionally, it is demonstrated that 3D printed sodium-ion hybrid capacitors deliver high energies/power densities of 81.4 Wh kg<sup>-1</sup>/0.32 mWh cm<sup>-2</sup> and 9992.1 W kg<sup>-1</sup>/38.76 mW cm<sup>-2</sup>, as well as applicability in a wide temperature range.

chemical energy storage (EES) systems, such as alkali-ion batteries (AIBs),<sup>[1–5]</sup> and supercapacitors (SCs),<sup>[6–10]</sup> represent a promising field for advancing research as well as practical applications. Generally, rechargeable batteries and supercapacitors differ in electrochemical storage mechanisms, thus featuring nearly inverse energy and power density characteristics. Nevertheless, nowadays, applications more and more require both high power and high energy simultaneously, which calls for the design of effective EES technologies for alleviating the trade-off between energy density and power density. Sodium-ion hybrid capacitors (SIHCs), by elaborately integrating the advantages of two types of storage systems (AIBs and SCs), have been demonstrated to have enormous possibilities for future energy storage devices that combine high energy density and high output power.<sup>[11–13]</sup> However, the pivotal hindrance in developing high-performance SIHCs is to surmount the kinetic imbalance between the sluggish Na<sup>+</sup> reaction kinetics in battery-type

anodes with the fast ion adsorption/desorption processes in capacitor-type cathodes.<sup>[14,15]</sup>


Among various alternative anodes for sodium-ion batteries, the conversion-type materials have the potential for realizing

## 1. Introduction

Triggered by urgent and various energy demands, ranging from portable electronic devices to stationary grid storages, electro-

W. Zong, G. J. Chao, T. X. Liu  
The Key Laboratory of Synthetic and Biological Colloids, Ministry of Education, School of Chemical and Material Engineering  
Jiangnan University  
Wuxi 214122, P. R. China  
E-mail: txliu@jiangnan.edu.cn

W. Zong, Y. Ouyang, L. L. Mo, C. Y. Zhou, Y.-E. Miao, T. X. Liu  
State Key Laboratory for Modification of Chemical Fibers and Polymer Materials  
College of Materials Science and Engineering  
Innovation Center for Textile Science and Technology  
Donghua University  
Shanghai 201620, P. R. China

 The ORCID identification number(s) for the author(s) of this article can be found under <https://doi.org/10.1002/adfm.202110016>.

DOI: 10.1002/adfm.202110016

H. L. Guo, J. Hofkens, F. L. Lai  
Department of Chemistry  
KU Leuven  
Celestijnenlaan 200F, Leuven 3001, Belgium  
E-mail: feili.lai@kuleuven.be

J. Hofkens  
Department of Molecular Spectroscopy  
Max Planck Institute for Polymer Research  
Ackermannweg 10, 55128 Mainz, Germany

Y. Xu, G. J. He, I. P. Parkin  
Christopher Ingold Laboratory  
Department of Chemistry  
University College London  
20 Gordon Street, London WC1H 0AJ, UK

W. Wang  
School of Metallurgical and Ecological Engineering  
University of Science and Technology Beijing  
Beijing 100083, China

both high storage capacity and high energy density concurrently, owing to their multi-electron redox reaction compared to the poor sodium storage performance of insertion-type materials.<sup>[16,17]</sup> As an emerging member in the family of 2D transition metal selenides (TMSels), rhenium diselenide (ReSe<sub>2</sub>) possesses disordered stacking layers with weak van der Waals interaction, which makes it favorable for Na<sup>+</sup> insertion/extraction and diffusion as a potential host candidate for sodium storage.<sup>[18–20]</sup> Unfortunately, the intrinsic low electronic conductivity and restricted accessibility of active sites in ReSe<sub>2</sub> bulk cause inferior electron transfer and sluggish ionic diffusion kinetics, respectively. Therefore, the development of appropriate TMSels-based hosts with fast electronic/ionic transfer kinetics may hold the key to optimize the electrochemical property for sodium-ion storage. It has been demonstrated that integrating TMSels materials with high-conductivity substrates, such as carbon nanofibers or graphene, is an effective strategy in relieving severe volume expansion, providing efficient ionic/electronic channels, and thereby enhancing electrochemical storage activities.<sup>[21–23]</sup> Unfortunately, the traditional physical blending process of active material and substrates leads to stacking of the individual components with poor intimate connection, which severely limits the interfacial charge-transfer capacity, especially at high charge/discharge rates. Recently, a number of approaches have been introduced to regulate and improve the interfacial contact between the two different components in a blend, such as 2D/2D assembled composites and strong bridging bonds.<sup>[24–26]</sup> Especially, the construction of strong bridging bonds at an atomic level is an effective way to enhance sodium storage performance due to the accelerated reaction kinetics with abundant as-created electron transport channels. However, it is still a great challenge to accurately control interface-bridging bonds in 2D TMSels. Furthermore, an in-depth understanding of the interaction mechanism associated with sodium storage performance is still lacking.

Apart from the great efforts in designing electrode materials, the employment of advanced manufacturing technologies also plays a vital role in improving energy storage performance. A prime example of such a manufacturing technique is extrusion-based 3D printing, which exhibits a high degree of freedom in process flexibility and structural design and enables manufacturing versatile structures with desired mechanical properties and functionalities.<sup>[27–31]</sup> Moreover, owing to the unique interconnected networks with periodic macropores, 3D-printed electrodes exhibit adequate mass transfer channels and electrode–electrolyte contact interfaces. Although 3D printing methods have been preliminarily employed in energy storage devices, such as supercapacitors,<sup>[32,33]</sup> lithium-ion batteries,<sup>[34]</sup> and sodium-ion batteries,<sup>[35]</sup> it has been challenging to realize good compatibility among multi-component inks to maximize the power and energy densities for completely 3D-printed hybrid capacitors devices.

Herein, we present a topochemistry-driven synthesis strategy for synthesizing 2D rhenium selenide intercalated by nitrogen-doped carbon (E-ReSe<sub>2</sub>@INC) through a molecular coordination-mediated approach. X-ray absorption spectroscopy analysis is used to dynamically track the coordination evolution from Re–O bonds to Re–C bonds at the heterointerface. The rational designed synthesis endows the hybrids with remarkable merits:

i) the intimate atomic interaction via strong Re–C bridging bonds at heterointerfaces between ReSe<sub>2</sub> and INC ensures a controllable interfacial coupling effect which can act as charge transfer channels for accelerated reaction kinetics; ii) the expanded interlayer-spacing due to weak van der Waals forces allows for fast Na<sup>+</sup> diffusion and provides abundant storage active sites; iii) a 0D–2D–3D configuration with interconnected porosity offers highly efficient mixed-transport pathways at three-phase boundaries (ReSe<sub>2</sub>, INC, and electrolyte). The E-ReSe<sub>2</sub>@INC electrode achieves improved high-rate capability (252.5 mAh g<sup>-1</sup> at 20 A g<sup>-1</sup>) and long-term cyclability (89.6% over 3500 cycles). Moreover, density functional theory (DFT) calculations reveal that the favorable Na<sup>+</sup> storage kinetics can be assigned to a low bonding energy of –0.06 eV and a low diffusion barrier of 0.08 eV. Additionally, the as-fabricated 3D-printed SIHCs deliver not only a high energy/power density of 81.4 Wh kg<sup>-1</sup>/0.32 mWh cm<sup>-2</sup> and 9992.1 W kg<sup>-1</sup>/38.76 mW cm<sup>-2</sup>, but can also perform over a wide temperature range (–20 °C to 50 °C).

## 2. Results and Discussion

The schematic procedures for the topochemical synthesis of the expanded 2D rhenium selenide intercalated by nitrogen-doped carbon (E-ReSe<sub>2</sub>@INC) material are illustrated in **Figure 1a**. The coordination-directed gelation process is conducted during the hydrothermal process, when the perrhenate ions coordinate with polyvinyl pyrrolidone (PVP) to generate expanded ReSe<sub>2</sub> layers mediated by PVP molecule chains, termed as E-ReSe<sub>2</sub>@PVP metal–polymer gel (E-ReSe<sub>2</sub>@PVP MPG). To evaluate the influence of the PVP, two additional samples with varying PVP amounts (E-ReSe<sub>2</sub>@PVP MPG-0.1 and E-ReSe<sub>2</sub>@PVP MPG-0.4) were prepared for subsequent comparison. All the E-ReSe<sub>2</sub>@PVP MPG samples displayed in inverted vials clearly illustrate the successful formation of gels (Figure S1, Supporting Information). Rheological measurements were studied to investigate the sol–gel transition behaviors of the as-obtained E-ReSe<sub>2</sub>@PVP MPG samples. Strain-sweeping measurements (Figure S2a, Supporting Information) show that the storage moduli (G′) are higher than the loss moduli (G″) for all MPG samples in the linear range from 0.01% to 1%. Meanwhile, the linear response of G′ and G″ can also be observed in the frequency range of 1–100 rad s<sup>-1</sup> (Figure S2b, Supporting Information), implying that all MPG samples are elastic-like solids. Additionally, the transformation strain of MPG sample increases with PVP content, indicating an enhanced intermolecular interaction of the gel network.<sup>[36–38]</sup> Therefore, the degree of coordination crosslinking network of the E-ReSe<sub>2</sub>@PVP MPG system firmly depends on the component ratio of metal to PVP. As verified by Fourier transform infrared (FT-IR) spectroscopy (Figure S3, Supporting Information), the peaks at ≈1655 and 1290 cm<sup>-1</sup> are assigned to the stretching vibrations of C=O and C–N bonds, respectively, demonstrating the intercalation of PVP in the framework of the as-synthesized ReSe<sub>2</sub>.<sup>[39]</sup>

Field-emission scanning electron microscopy (FESEM) images (Figures S4 and S5, Supporting Information) reveal that the E-ReSe<sub>2</sub>@PVP MPG exhibits a unique 3D interconnected network with simulating aerogel structures in the micron range.<sup>[40,41]</sup> Subsequently, the E-ReSe<sub>2</sub>@PVP MPG could be



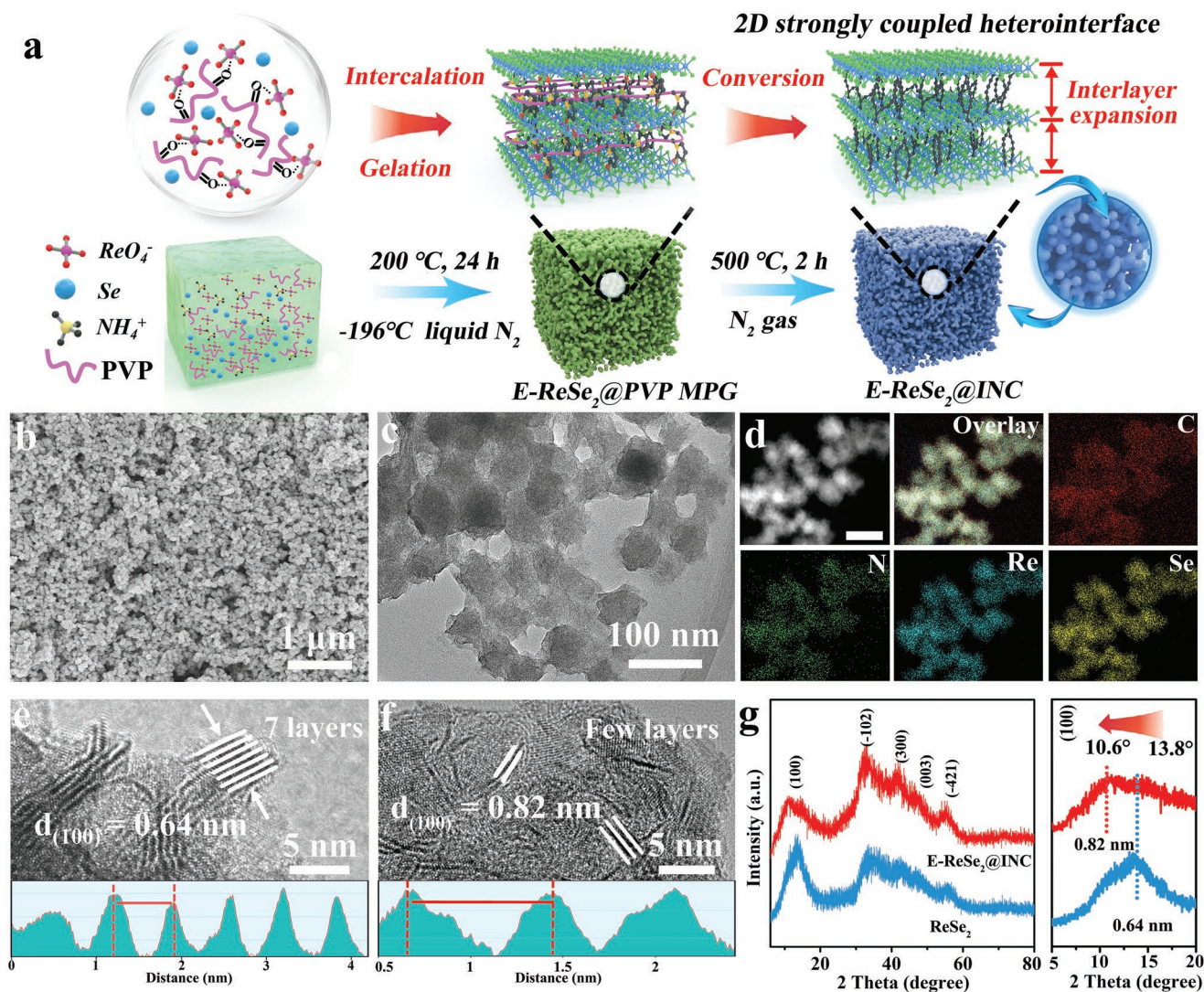


**Figure 1.** Structural characterization of E-ReSe<sub>2</sub>@INC. a) Schematic diagram of the topochemistry-driven synthesis of E-ReSe<sub>2</sub>@INC. b) FESEM image and c) TEM image of E-ReSe<sub>2</sub>@INC. d) EDX elemental mappings of E-ReSe<sub>2</sub>@INC. The scale-bar is 100 nm. HRTEM images of e) ReSe<sub>2</sub> bulk and f) E-ReSe<sub>2</sub>@INC. g) XRD patterns of ReSe<sub>2</sub> bulk and E-ReSe<sub>2</sub>@INC.

changed into E-ReSe<sub>2</sub>@INC after a freeze-drying and annealing treatment, where the resulting ReSe<sub>2</sub> layer further facilitates converting the polymer molecules into carbon by reverse catalysis.<sup>[42]</sup> Notably, the 3D interconnected quasi-aerogel structure could be well retained in E-ReSe<sub>2</sub>@INC (Figure 1b) during the annealing process, which is mainly attributed to the robust coordination-bonding network among the E-ReSe<sub>2</sub>@PVP MPG. The bulk ReSe<sub>2</sub> sample, in contrast, shows irregular morphology with severe aggregations (Figure S6, Supporting Information). The transmission electron microscopy (TEM) image further demonstrates that the multi-dimensional architecture of the E-ReSe<sub>2</sub>@INC composite is composed of abundant interconnected subunits with a narrow size distribution and good dispersity (Figure 1c). The energy-dispersive X-ray (EDX) spectrometry mappings from high-angle annular dark-field (HAADF) TEM images (Figure 1d) demonstrate that the C, N, Re, and Se elements are homogeneously distributed throughout the E-ReSe<sub>2</sub>@INC (Figure S7, Supporting Information).

The high-resolution TEM (HR-TEM) image (Figure 1e) shows that the ReSe<sub>2</sub> bulk tends to aggregate into stacked ReSe<sub>2</sub> layers with *d*-spacing of 0.64 nm, while the stacking of the 2D E-ReSe<sub>2</sub> layers in E-ReSe<sub>2</sub>@INC is significantly expanded with an interlayer spacing of 0.82 nm (Figure 1f), offering incontestable evidence of the successful intercalation of carbon in the ReSe<sub>2</sub> layers. Moreover, the X-ray diffraction (XRD) patterns (Figure 1g) show that the peak assigned to the (100) diffraction of ReSe<sub>2</sub> shifts to a lower position, from 13.8° for ReSe<sub>2</sub> bulk to 10.6° for E-ReSe<sub>2</sub>@INC, further demonstrating the expansion of the interlayer spacing from 0.64 to 0.82 nm, which is in good agreement with the HRTEM observations.

X-ray photoelectron spectroscopy (XPS) measurements were conducted to probe the chemical composition and valence states of E-ReSe<sub>2</sub>@INC. XPS survey spectra reveal that both E-ReSe<sub>2</sub>@PVP MPG and E-ReSe<sub>2</sub>@INC consist of Re, Se, C, and N elements (Figures S8 and S9, Supporting Information). As depicted in Figure 2a, the Re 4f XPS spectrum of E-ReSe<sub>2</sub>@INC

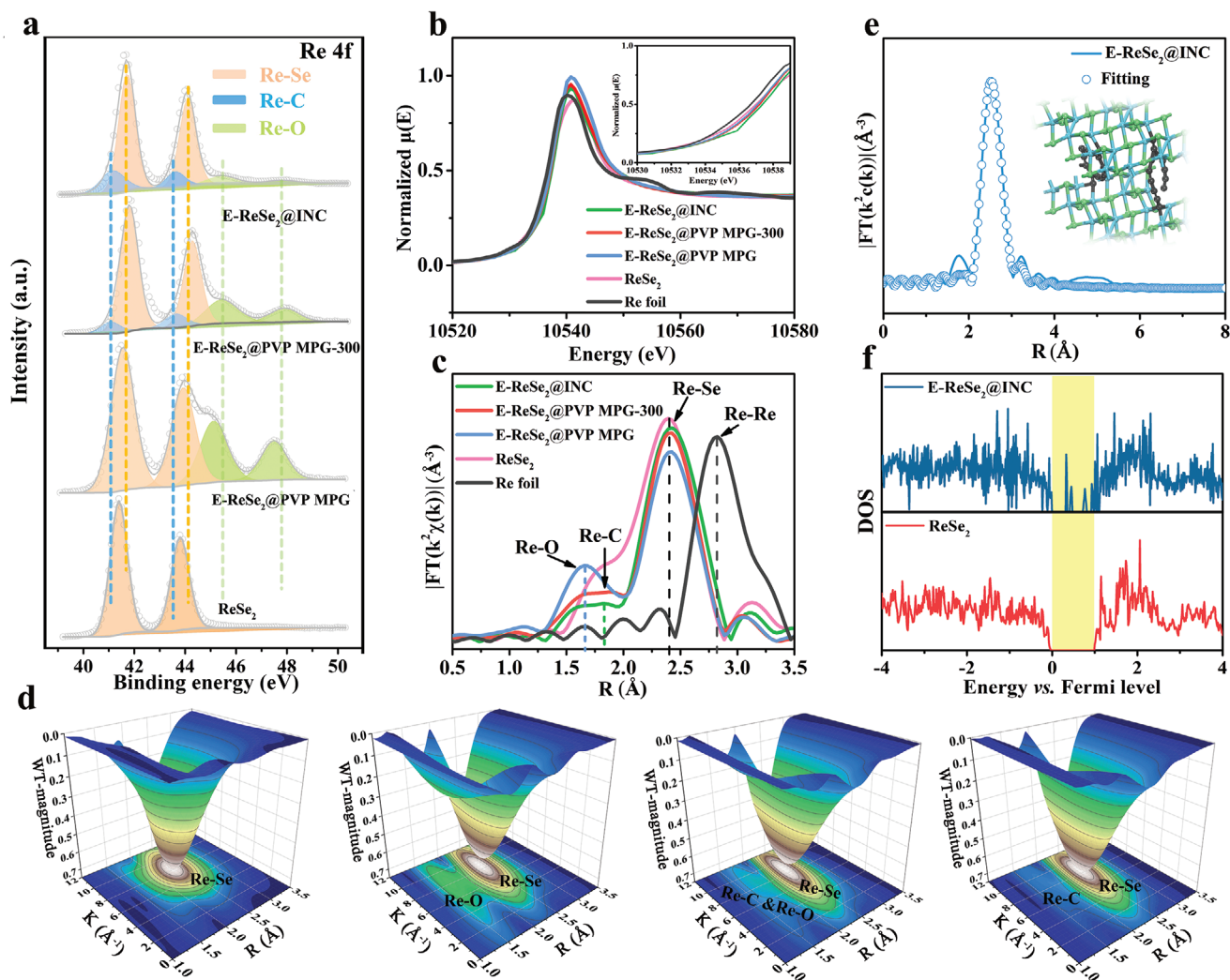


**Figure 2.** Ex situ characterization of coordination structure and DFT calculation. a) High-resolution XPS Re 4f spectra of ReSe<sub>2</sub>, E-ReSe<sub>2</sub>@PVP MPG, E-ReSe<sub>2</sub>@PVP MPG-300, and E-ReSe<sub>2</sub>@INC. b) XANES spectra (inset: enlarged view of the absorption edge position) and c) FT-EXAFS spectra of Re foil, ReSe<sub>2</sub>, E-ReSe<sub>2</sub>@PVP MPG, E-ReSe<sub>2</sub>@PVP MPG-300, and E-ReSe<sub>2</sub>@INC at Re L<sub>3</sub>-edges. d) WT-EXAFS at Re L<sub>3</sub>-edges of ReSe<sub>2</sub>, E-ReSe<sub>2</sub>@PVP MPG, E-ReSe<sub>2</sub>@PVP MPG-300, and E-ReSe<sub>2</sub>@INC. e) The Re L<sub>3</sub>-edges EXAFS fitting curves for E-ReSe<sub>2</sub>@INC at R-space. (The inset: the schematic models of E-ReSe<sub>2</sub>@INC. Atom colors: royal blue, Re; green, Se; dark gray, C. f) Calculated DOS for E-ReSe<sub>2</sub>@INC and ReSe<sub>2</sub>.

shows two peaks at 41.8 and 44.2 eV, corresponding to the core 4f<sub>7/2</sub> and 4f<sub>5/2</sub> peaks for Re<sup>4+</sup>, respectively, which are higher than those of ReSe<sub>2</sub> bulk (Re 4f<sub>7/2</sub>: 41.3 eV and Re 4f<sub>5/2</sub>: 43.8 eV), indicating the lower electronic density of the Re center in E-ReSe<sub>2</sub>@INC.<sup>[43]</sup> Besides, two other obvious peaks at ≈45.4 and ≈47.9 eV originate from the Re–O bond in E-ReSe<sub>2</sub>@PVP MPG and E-ReSe<sub>2</sub>@PVP MPG-300 (E-ReSe<sub>2</sub>@PVP MPG under 300 °C annealing treatment), which derive from the coordination in the metal–polymer gel networks. The contribution of the Re–O bonds increases gradually from the E-ReSe<sub>2</sub>@PVP MPG-0.1 sample to the E-ReSe<sub>2</sub>@PVP MPG-0.4 sample, due to an increased content of Re–O coordination (Figure S10, Supporting Information). This result is in accordance with the rheological behavior of increasing transformation strain, which confirms the enhanced intermolecular interaction of the MPG network once again. Noticeably, both E-ReSe<sub>2</sub>@INC and E-ReSe<sub>2</sub>@PVP MPG-300 show a new pair of peaks around 41.1

and 43.6 eV, which are related to the Re–C bond at the interface of the ReSe<sub>2</sub>/INC heterostructure. It is interesting that the content of Re–O bond gradually decreases, accompanied by the emergence of the Re–C bond, indicating the presence of the transition process from Re–O coordination to Re–C coordination as the temperature increases.

To gain insight into the topological structure of E-ReSe<sub>2</sub>@INC, X-ray absorption spectroscopy (XAS) was conducted to further explore the structural evolution and local coordination environment during the annealing treatment. In the Re L<sub>3</sub>-edge X-ray absorption near-edge structure (XANES), the E-ReSe<sub>2</sub>@INC exhibits a slightly higher absorption edge position in comparison with ReSe<sub>2</sub> bulk, which demonstrates the electron deficiency at Re atoms and solid interactions between heteronuclear Re atoms and the INC support (Figure 2b). As the k<sub>3</sub>-weighted Fourier transform (FT)-EXAFS spectra at Re L<sub>3</sub>-edge shown in Figure 2c, there is a main peak at ≈2.42 Å

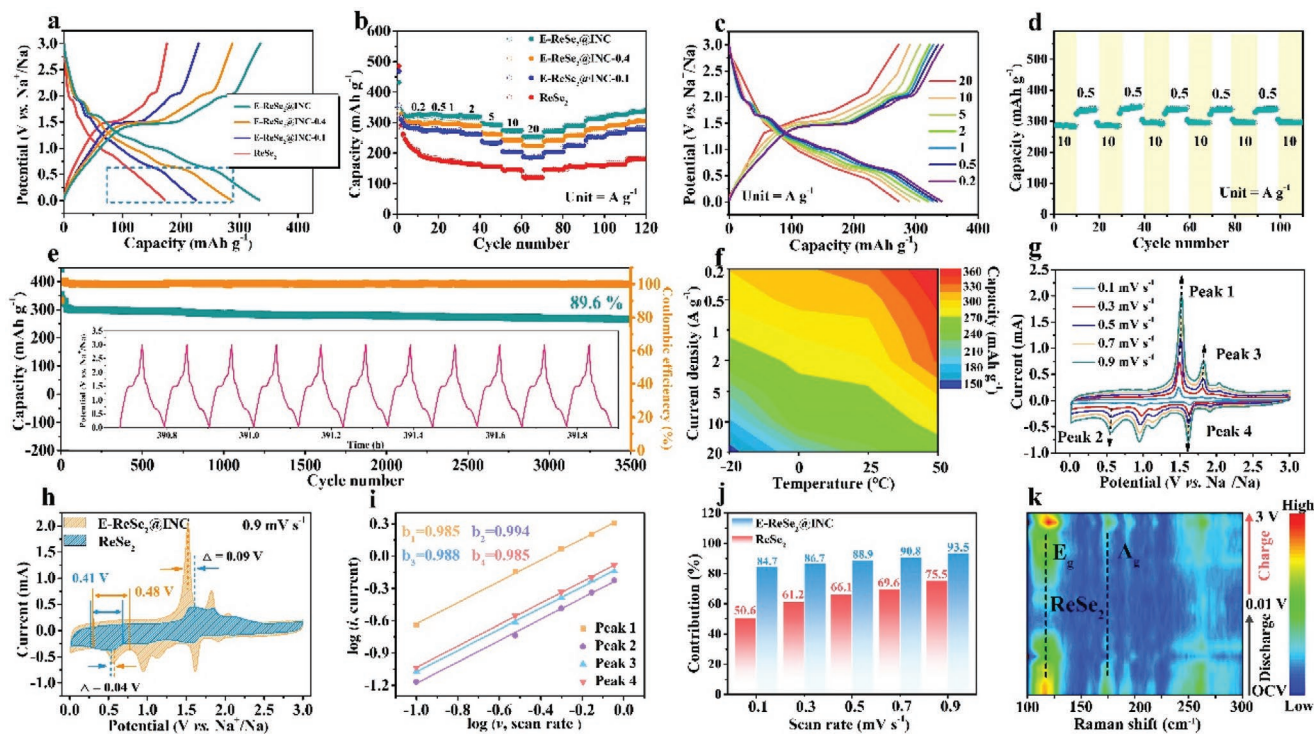


for all samples, which can be attributed to the scattering path of the Re–Se bond. Moreover, no apparent peaks at 2.82 Å for Re–Re bonds are detected compared with Re foil, confirming the absence of Re nanoparticles in the E-ReSe<sub>2</sub> component. As expected, in comparison to ReSe<sub>2</sub> bulk, E-ReSe<sub>2</sub>@PVP MPG has two main peaks at 2.42 and 1.66 Å, which can be attributed to scattering paths of Re–Se and Re–O bonds, respectively. Moreover, the E-ReSe<sub>2</sub>@PVP MPG-300 and E-ReSe<sub>2</sub>@INC exhibit new peaks at ≈1.84 Å, which can be attributed to the scattering path of the Re–C bond. The wavelet transform of  $c(k)$  (WT)-EXAFS is an intuitive way to demonstrate the properties of adjacent Re atoms (Figure 2d; Figure S11, Supporting Information). The E-ReSe<sub>2</sub>@PVP MPG and E-ReSe<sub>2</sub>@PVP MPG-300 show two distinct scattering path signals at [ $\chi$  (k),  $\chi$  (R)] of [8.1, 1.66] and [8.5, 2.42], which are associated with the Re–O and Re–Se paths, respectively. The intensity of the Re–O path signals in E-ReSe<sub>2</sub>@PVP MPG-300 attenuates and one scattering path signal appears at [8.8, 1.84], resulting from the Re–C path. Moreover, E-ReSe<sub>2</sub>@INC only displays two scattering path signals at [8.5, 2.42] and [8.8, 1.84] corresponding to the Re–Se and Re–C paths, respectively, which are consistent with the Re L<sub>3</sub>-edge FT-EXAFS results. Unambiguously, by combining the FT- and WT-EXAFS results at the Re L<sub>3</sub>-edge, part of the Re atoms are confirmed to be connected with C atoms and generate Re–C bonds in E-ReSe<sub>2</sub>@INC, which are derived from the transformation of Re–O bonds in E-ReSe<sub>2</sub>@PVP MPG. To determine the coordination environment of different samples, we employed DFT calculations to deduce structural models, based on the FT-EXAFS experimental spectra and fitting curves. The EXAFS fitting results show that the Re atom in E-ReSe<sub>2</sub>@INC has two coordinating interactions of the Re–Se bond and the Re–C bond. The EXAFS fitting curves at R-space (Figure 2e) and k-space are consistent with experiment spectra of E-ReSe<sub>2</sub>@INC (Figures S12 and S13, Supporting Information).<sup>[44]</sup> Next, possible E-ReSe<sub>2</sub>@INC models were further constructed and optimized by DFT calculations based on the corresponding coordination configuration. For the E-ReSe<sub>2</sub>@INC, the Re–Se and Re–C path lengths are ≈2.45 Å and 2.15 Å (Figure S14, Supporting Information), respectively, in good agreement with EXAFS fitting data (Table S1, Supporting Information). In addition, according to the calculated density of states (DOS), the ReSe<sub>2</sub> bulk shows characteristics of an indirect bandgap semiconductor with wide bandgap (0.97 eV). The bandgap observably decreased to 0.31 eV for E-ReSe<sub>2</sub>@INC, a signature for more charge carriers and enhanced inherent conductivity (Figure 2f). Therefore, a strong-coupled interface is constructed at the interface between the ReSe<sub>2</sub> layer and INC support via Re–C bridging bonds, which enables controllable interfacial effects and acts as an electron transport channel for accelerating the reaction kinetics. Moreover, the N and C contents of all the above materials were quantitated by using elemental analysis (Table S2, Supporting Information).

To evaluate the possible role of the strong-coupled interaction in E-ReSe<sub>2</sub>@INC, the sodium storage properties of various samples (derived from E-ReSe<sub>2</sub>@PVP MPG with different component ratio of metal/PVP) were investigated. Figure 3a shows the galvanostatic charge–discharge (GCD) profiles for various E-ReSe<sub>2</sub>@INC samples and the ReSe<sub>2</sub> bulk sample as a reference, with a potential range of 0.01–3.0 V. The E-ReSe<sub>2</sub>@INC

shows the elongated plateau length at 1.5 V and much smaller polarization compared to those of E-ReSe<sub>2</sub>@INC-0.1, E-ReSe<sub>2</sub>@INC-0.4, and ReSe<sub>2</sub> bulk, indicating its highly improved reaction kinetics for the sodiation/desodiation process. As shown in Figure 3b, the E-ReSe<sub>2</sub>@INC delivers initial charge/discharge capacities of 349.3/431.5 mAh g<sup>−1</sup> at 0.2 A g<sup>−1</sup> with the highest initial coulombic efficiency (ICE) of 80.9% when compared to E-ReSe<sub>2</sub>@INC-0.1 (76.1%), E-ReSe<sub>2</sub>@INC-0.4 (71.8%), and ReSe<sub>2</sub> bulk (69.6%). And, the comparison of rate capabilities for various E-ReSe<sub>2</sub>@INC samples and ReSe<sub>2</sub> bulk is presented at variable current densities from 0.2 to 20 A g<sup>−1</sup>. Remarkably, the E-ReSe<sub>2</sub>@INC shows reversible capacities of 327.3, 323.8, 321.4, 319.9, 294.4, and 272.7 mAh g<sup>−1</sup> at various current densities from 0.2 to 10.0 A g<sup>−1</sup>. A considerable capacity retention of 77.1% (reversible capacity of 252.5 mAh g<sup>−1</sup>) can still be maintained even at a high density of 20 A g<sup>−1</sup>. Furthermore, GCD curves of E-ReSe<sub>2</sub>@INC exhibit obvious charge/discharge plateau at all current densities from 0.2 to 20 A g<sup>−1</sup>, demonstrating its superior reversibility of redox reactions compared to other samples (Figure 3c; Figure S15, Supporting Information). Furthermore, the capacities of E-ReSe<sub>2</sub>@INC could be kept stable without any fading at successive fluctuating current densities of 10 and 0.5 A g<sup>−1</sup> (Figure 3d), a manifestation of its fast reversible abilities. Generally, at the high-rate state, the electron/ion would be only deposited on the surface of active material without a sufficient reaction, finally giving rise to the steep lowering of voltage and severe polarization. The superior heterointerface in E-ReSe<sub>2</sub>@INC via Re–C bonds enables its function as an electron-transferring bridge, as 0D–2D–3D multi-dimensional structure elements are united to provide mixed electron/ion pathway from the exterior into the interior along the whole electrode, and achieve fast kinetics during the sodiation/desodiation process. Figure 3e confirms the stable cycling life of E-ReSe<sub>2</sub>@INC at a current density of 10.0 A g<sup>−1</sup>, which can maintain a capacity of 272.8 mAh g<sup>−1</sup> with a satisfactory capacity retention of 89.6% after 3500 cycles. By detecting the plateaus from the 2990th to 3000th cycle, the similarity of the shapes of GCD profiles also proves its stable reversible reaction in long-term cycling (inset in Figure 3e). Moreover, the rate capabilities of E-ReSe<sub>2</sub>@INC outperform those of previously reported materials for sodium storage (Figure S16 and Table S3, Supporting Information). Apart from a superior rate capability at ambient conditions, the wide-temperature range sodium-storage performance of E-ReSe<sub>2</sub>@INC was evaluated from 50 °C to −20 °C. The GCD profiles at 0.5 A g<sup>−1</sup> exhibit consistent charge/discharge plateaus at all testing temperatures (Figure S17, Supporting Information). The E-ReSe<sub>2</sub>@INC indeed shows satisfactory storage capacity at various current densities and operating temperatures (Figure 3f). For instance, at a current density of 0.2 A g<sup>−1</sup>, the reversible capacity retention is ≈90.4%, 86.2%, and 84.6% at 25, 0, and −20 °C, respectively, as compared to the reversible capacity of 355.6 mAh g<sup>−1</sup> at 50 °C. This proves the weak temperature dependence of the E-ReSe<sub>2</sub>@INC (Figures S18 and S19, Supporting Information).<sup>[45,46]</sup>

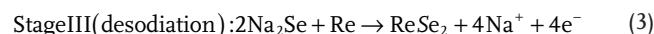
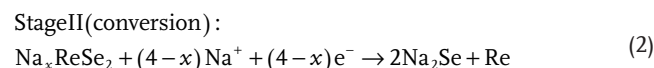
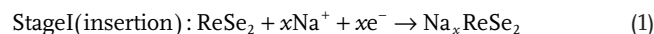
A reaction kinetic analysis based on cyclic voltammetry (CV) curves was performed to provide insight into the charge storage mechanisms. As demonstrated in Figure 3g, all CV curves of E-ReSe<sub>2</sub>@INC exhibit well-maintained shapes at increasing sweep rates (0.1 to 0.9 mV s<sup>−1</sup>), similar to ReSe<sub>2</sub> bulk and



**Figure 3.** Electrochemical characterization of E-ReSe<sub>2</sub>@INC. a) GCD profiles and b) rate capability of E-ReSe<sub>2</sub>@INC-0.1, E-ReSe<sub>2</sub>@INC, E-ReSe<sub>2</sub>@INC-0.4, and ReSe<sub>2</sub> bulk. Here, the solid and hollow points present discharge and charge processes, respectively. c) GCD curves of E-ReSe<sub>2</sub>@INC at different current densities. d) The reversibility of E-ReSe<sub>2</sub>@INC at current densities of 0.5 and 10 A g<sup>-1</sup>. e) The long-term cycling stability of E-ReSe<sub>2</sub>@INC (Inset: GCD profiles from 2990th to 3000th loops). f) Capacity retention variations along with current density and temperature. g) CV curves at stepwise scan rates (0.1 to 0.9 mV s<sup>-1</sup>) of E-ReSe<sub>2</sub>@INC. h) The comparison between CV curves of E-ReSe<sub>2</sub>@INC and ReSe<sub>2</sub> bulk at 0.9 mV s<sup>-1</sup>. i) The relation between log(*i*) and log(*v*) of E-ReSe<sub>2</sub>@INC. j) Normalized capacitance contribution proportions at different scan rates of E-ReSe<sub>2</sub>@INC and ReSe<sub>2</sub> bulk. k) In situ Raman spectra of E-ReSe<sub>2</sub>@INC during the first discharge/charge process.

E-ReSe<sub>2</sub>@INC-0.1/0.4 (Figure S20, Supporting Information). As compared to the CV curves of E-ReSe<sub>2</sub>@INC and ReSe<sub>2</sub> bulk at 0.9 mV s<sup>-1</sup> (Figure 3h), taking the main oxidation/reduction peak (denoted as Peak 1/Peak 2) as an example, the reduced voltage difference (between Peak 1 and Peak 2) of E-ReSe<sub>2</sub>@INC indicates a low electrode polarization. Figure S21, Supporting Information, exhibits the linear relationship between *I<sub>p</sub>* and *v*<sup>1/2</sup>, where the values of the slope are 2.82/−0.87 for E-ReSe<sub>2</sub>@INC and 0.53/−0.49 for ReSe<sub>2</sub> bulk. From this, their diffusion coefficient (*D*) can be calculated. The *D* of Peak 1/Peak 2 is 8.57 × 10<sup>-8</sup>/8.18 × 10<sup>-9</sup> cm<sup>2</sup> s<sup>-1</sup> for E-ReSe<sub>2</sub>@INC and 2.91 × 10<sup>-9</sup>/3.31 × 10<sup>-9</sup> cm<sup>2</sup> s<sup>-1</sup> for ReSe<sub>2</sub> bulk. Obviously, the larger *D* values of E-ReSe<sub>2</sub>@INC imply its faster sodium ion diffusion. According to the relationship between the *i* and *v* obtained from the CV curves, the value of slope *b* can be calculated by the following equation:  $i = a v^b$  and  $\log(i) = b \log(v) + \log(a)$ , where *a* and *b* are variable parameters obtained by the linear relation between the log(*i*) and log(*v*). Generally, if *b* approaches 0.5, that corresponds to a diffusion-dominated behavior, whereas when *b* is close to 1.0, a pseudocapacitive behavior is the main charge storage process.<sup>[47,48]</sup> As shown in Figure 3i, the *b*-values of E-ReSe<sub>2</sub>@INC determined by the slopes of Peaks 1–4 are 0.985, 0.994, 0.988, and 0.985, respectively, demonstrating the predominant occurrence of pseudocapacitive sodium storage. Moreover, the increased *b*-values of E-ReSe<sub>2</sub>@INC over those of the ReSe<sub>2</sub> bulk (Figure S22, Supporting Information), reveal the enhanced capacitive kinetics of the former

material. This in turn proves that the presence of a 0D–2D–3D architecture and the Re–C bridging bonds can bring about an improvement in pseudocapacitive behaviors. More specifically, the total capacitive (*k<sub>1</sub>v*) and diffusion (*k<sub>2</sub>v*<sup>1/2</sup>) contributions can be quantitatively determined by a given scan rate according to the equation:  $i/v^{1/2} = k_1 v^{1/2} + k_2$ . The pseudocapacitive contributions are quantified as capacitive contribution at 0.9 mV s<sup>-1</sup>, which is 93.5% for E-ReSe<sub>2</sub>@INC and 75.5% for ReSe<sub>2</sub> bulk (Figure S23, Supporting Information). With increasing scan rates, the fraction of capacitive contribution increases, while the fraction of diffusive control decreases. The E-ReSe<sub>2</sub>@INC presents a higher fraction of the capacitive contribution at different scan rates, pointing toward the origin of its outstanding rate capability (Figure 3j). To confirm the reaction processes and possible crystal evolutions under different voltages during the sodiation/desodiation processes, a series of in situ Raman, ex situ XRD, and HRTEM were carried out (Figure 3k; Figure S24, Supporting Information), from which the reaction mechanism at different GCD states can be described as follows:





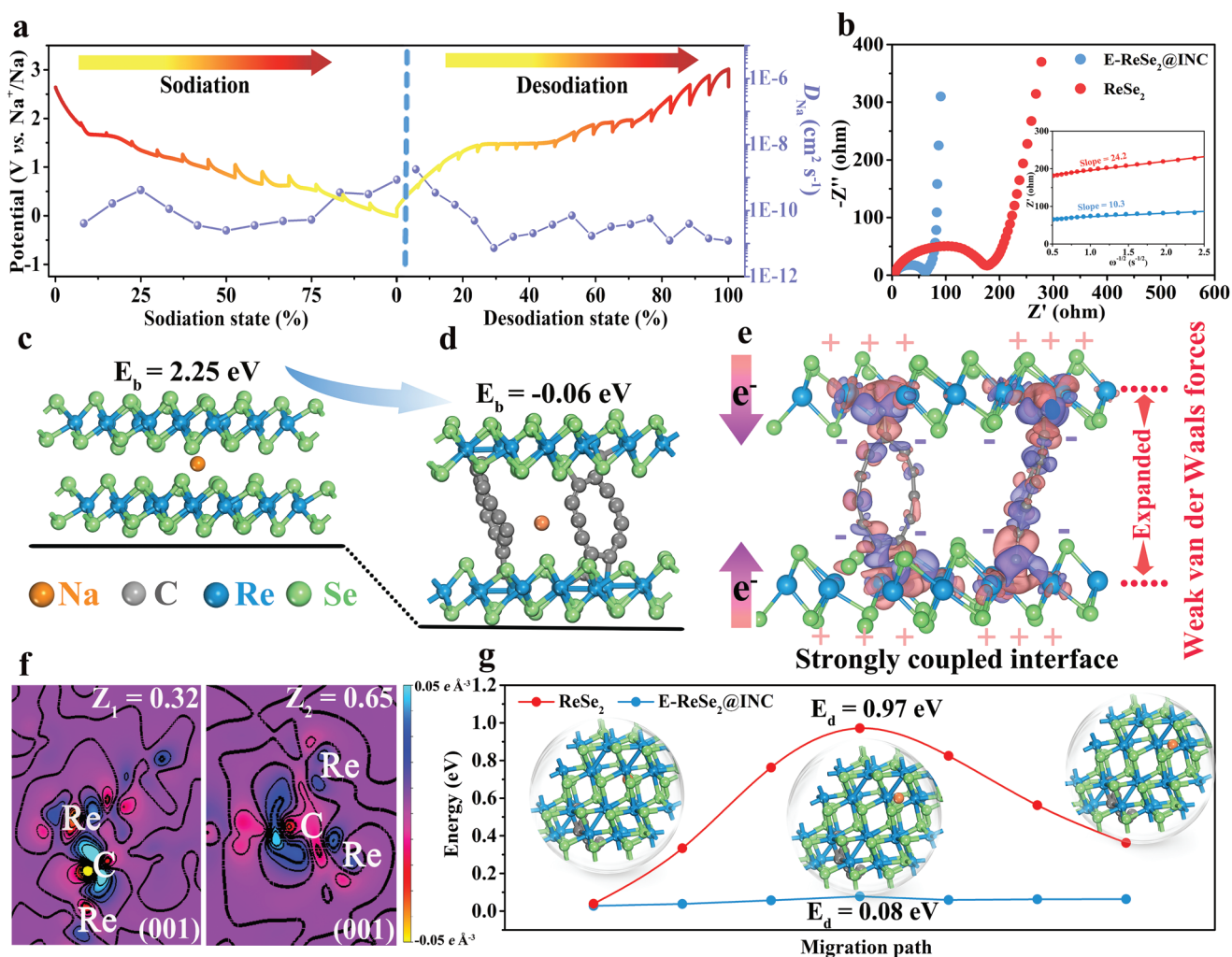


**Figure 4.** Electrochemical characterization of ion diffusion and DFT calculation. a) GITT potential profiles and corresponding ion diffusion coefficients for E-ReSe<sub>2</sub>@INC. b) Nyquist plots of E-ReSe<sub>2</sub>@INC and ReSe<sub>2</sub> bulk (Inset: plots of  $\omega^{-1/2}$  vs  $Z'$ ). The atomic models with one bonded sodium ion in c) ReSe<sub>2</sub> and d) E-ReSe<sub>2</sub>@INC, as well as corresponding bonding energy values. e) The charge density difference of E-ReSe<sub>2</sub>@INC (pink area: electron accumulation; purple area: electron depletion) and f) 2D contour map in (001) section of E-ReSe<sub>2</sub>@INC. g) The corresponding migration energy barriers in E-ReSe<sub>2</sub>@INC and ReSe<sub>2</sub> (inset: the minimum energy pathways for Na<sup>+</sup> diffusion through the E-ReSe<sub>2</sub>@INC).

The ion diffusion kinetics during electrochemical process was further studied by the galvanostatic intermittent titration technique (GITT) measurements. It can be viewed from **Figure 4a** that the E-ReSe<sub>2</sub>@INC possesses higher Na<sup>+</sup> diffusion coefficients than the ReSe<sub>2</sub> bulk (Figure S25, Supporting Information), indicating its superior sodium ion diffusion kinetics. Meanwhile, we measured electrochemical impedance spectroscopy (EIS) for both E-ReSe<sub>2</sub>@INC and ReSe<sub>2</sub> (Figure 4b), where the charge transfer resistance ( $R_{ct}$ ) in E-ReSe<sub>2</sub>@INC (62.1 ohms) is considerably lower than for ReSe<sub>2</sub> bulk (178.4 ohms). In the low-frequency region, the steeper slope gradient of E-ReSe<sub>2</sub>@INC implies its capacitive-like behavior and accelerated sodium ion diffusion. The results further underscore the improved charge and ion transfer efficiency of E-ReSe<sub>2</sub>@INC. DFT calculations were further conducted to address how the interfacial engineering affects the Na<sup>+</sup> storage kinetics. After optimizing the structural models of ReSe<sub>2</sub> and E-ReSe<sub>2</sub>@INC with Na<sup>+</sup> insertion (Figure 4c,d), their bonding energy

values are 2.25 and  $-0.06$  eV for ReSe<sub>2</sub> and E-ReSe<sub>2</sub>@INC, respectively, indicating that the strongly coupled interface between the ReSe<sub>2</sub> layer and the INC results in the enhanced ion storage property for Na ions. Next, the charge density difference and corresponding 2D slices depict the electronic transfer states at the interface between ReSe<sub>2</sub> and INC components in detail (Figure 4e–g). More specifically, the electrons of the neighboring Re atoms are inclined to flow toward INC with higher electronegativity via the “bridge” formed by the Re–C bonds at the heterogeneous interface, resulting in positive charges on Re atoms and enhanced electron density on the INC support. This result reveals a so called “strong bridging-bonds-induced interface effect” that can accelerate electron transfer, leading to enhanced electrical conductivity compared to ReSe<sub>2</sub>, in accordance with the EIS results (Figure 4b). Meanwhile, these theoretical results are in excellent agreement with the XPS and XAS results (Figure 2a,b) as partial electrons of Re centers have been delocalized from ReSe<sub>2</sub> to INC. Due to the strong interface

effect and the resulting electron transfer between ReSe<sub>2</sub> and INC, abundant active sites are formed in the close vicinity of ReSe<sub>2</sub> for Na<sup>+</sup> storage. The intercalated N-doped carbon layer further acts as the “pillar” component between the ReSe<sub>2</sub> layers, which weakens the van der Waals forces and affords larger interlayer spacing opportunities for efficient diffusion of large ions without significant volume collapse. Notably, our calculations confirm that the energy barrier for Na<sup>+</sup> migration into ReSe<sub>2</sub> through the E-ReSe<sub>2</sub>@INC boundary with an expanded distance is 0.08 eV, which is considerably lower than that for Na<sup>+</sup> migration across a more confined stacked ReSe<sub>2</sub> edge (0.97 eV). The heterointerface connected via Re–C bonds of E-ReSe<sub>2</sub>@INC is thus imperative to create open channels for Na<sup>+</sup> entry into ReSe<sub>2</sub> layer, leading to an improved D<sub>Na</sub> for high-rate operation.

Given the discussions above, the E-ReSe<sub>2</sub>@INC nano-architecture affording predominant pseudocapacitive Na<sup>+</sup>

storage is appropriate to construct SIHCs devices and meet the growing practical demand. As an emerging additive manufacturing method, extrusion-based 3D printing technology can be used to manufacture SIHCs devices with customized architectures (Figure 5a). To guarantee a favorable 3D printing process of electrodes targeting high-performance SIHCs devices (3DP-SIHCs), the rheological behavior of the as-obtained E-ReSe<sub>2</sub>@INC/carbon nanotube (CNT)/graphene oxide (GO) ink and active carbon (AC)/CNT/GO ink was evaluated. As shown in Figure 5b, both the E-ReSe<sub>2</sub>@INC/CNT/GO and AC/CNT/GO inks display appropriate apparent viscosities and shear-thinning behaviors as non-Newtonian fluids, allowing for continuous flow of printable inks under extrusion processing. The behavior for both E-ReSe<sub>2</sub>@INC/CNT/GO and AC/CNT/GO inks can be well explained by the Herschel–Bulkley model:  $\tau = \eta(\dot{\zeta}) \dot{\zeta} = \tau_y + K\dot{\zeta}^n$ ,

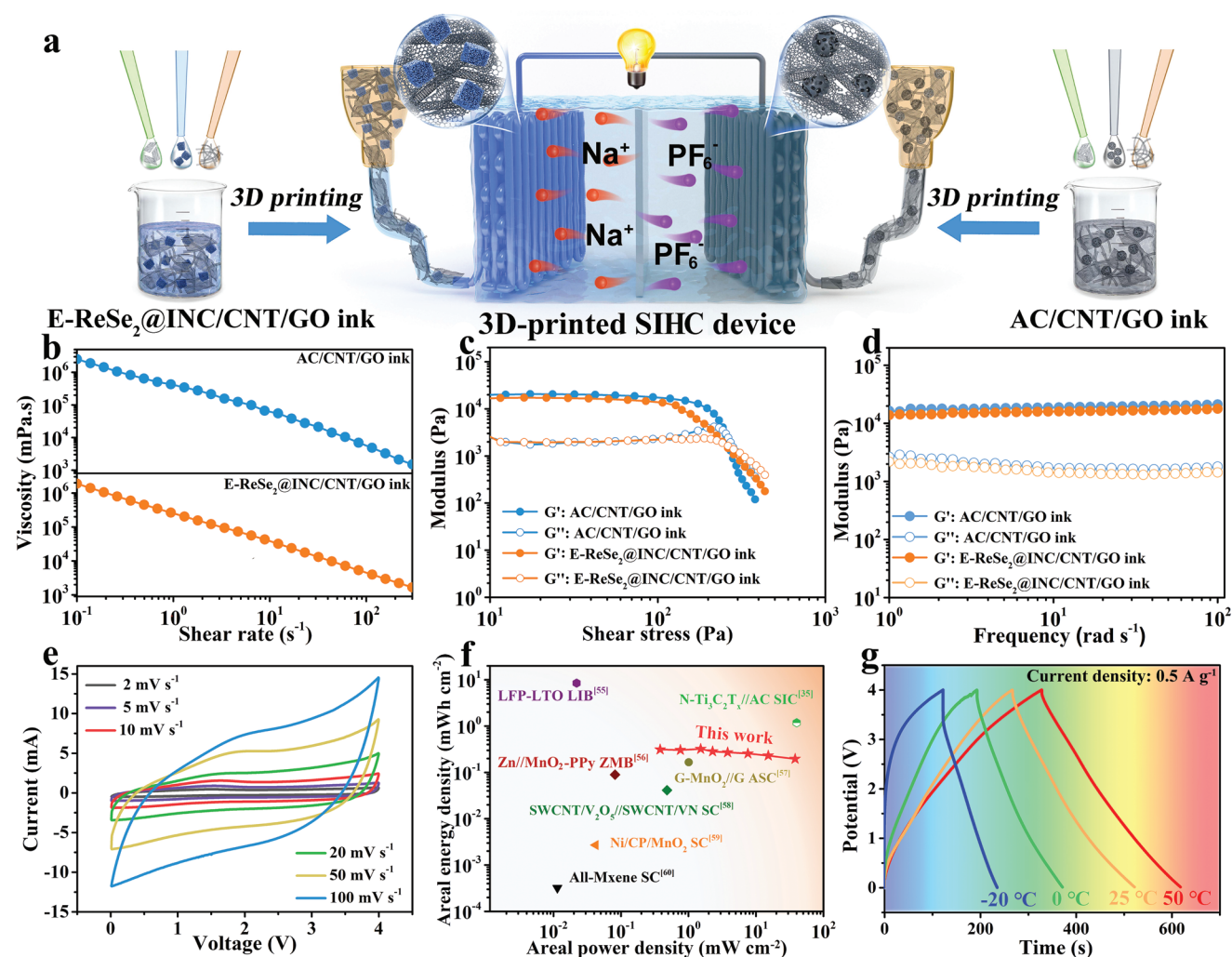


**Figure 5.** Fabrication of E-ReSe<sub>2</sub>@INC//AC 3DP-SIHCs. a) Schematic illustration for E-ReSe<sub>2</sub>@INC//AC 3DP-SIHCs device and corresponding charge process. b) The apparent viscosity as a function of shear rate. c) Storage modulus and loss modulus as a function of shear stress d) Dynamic modulus (G' and G'') as a function of frequency for E-ReSe<sub>2</sub>@INC/CNT/GO and AC/CNT/GO inks. e) CV curves at stepwise scan rates of E-ReSe<sub>2</sub>@INC//AC 3DP-SIHCs. f) Ragone plots of the E-ReSe<sub>2</sub>@INC//AC 3DP-SIHCs in comparison with other reported energy storage devices. g) GCD curves tested at 0.5 A g<sup>-1</sup> of 3DP-SIHCs device at various temperatures.



where  $\tau$ ,  $\eta$ ,  $\xi$ ,  $\tau_y$ , and  $n$  represent shear stress, apparent viscosity, shear rate, yield stress, and a power-law exponent, respectively.<sup>[49,50]</sup>

Figure 5c presents the  $G'$  and  $G''$  plots of as-obtained ink as a function of shear stress:  $G' > G''$  before the yield stress point (the point of intersection of the  $G'$  and  $G''$ ), as is typical for conventional elastic-like solids, and  $G' > G''$  after the yield stress point, as is typical for liquid-like behavior in viscoelastic materials. These rheological properties ensure that the E-ReSe<sub>2</sub>@INC/CNT/GO and AC/CNT/GO inks can be extruded smoothly under shear stress to achieve a stable flow of ink without blockage during the extrusion printing process. Furthermore, Figure 5d depicts that  $G'$  is higher than  $G''$  for the as-obtained inks throughout the frequency range of 0.01–100 rad s<sup>-1</sup>, proving their viscoelastic property with typical gel in the static state. As demonstrated by the frequency-independent modulus curves, a robust 3D network framework can be constructed within the as-obtained inks to stabilize long-term dispersion stability at rest.<sup>[51–54]</sup> Hence, the rheological behaviors of the E-ReSe<sub>2</sub>@INC/CNT/GO and AC/CNT/GO inks allow for printing 3DP-SIHCs devices without deformation. Figure S26, Supporting Information, shows the various digital photos of customized-printed patterns on the polyethylene terephthalate (PET) substrate, confirming shape diversity and wide versatility. Considering the operational voltage windows of the CV curves for the E-ReSe<sub>2</sub>@INC and AC electrodes (Figure S27, Supporting Information), the E-ReSe<sub>2</sub>@INC//AC 3DP-SIHCs was operated under a suitable working voltage (0.01 to 4 V) to avoid the decomposition of the electrolytes and other side reactions. Under operation in 3DP-SIHCs devices, the electrochemical properties of E-ReSe<sub>2</sub>@INC were further demonstrated, exhibiting a superior specific capacitance of 36.9 F g<sup>-1</sup> (118.8 mF cm<sup>-2</sup>) compared to conventional blade-casting electrodes (C-SIHC) of 29.1 F g<sup>-1</sup> (76.7 mF cm<sup>-2</sup>). The enhanced electrochemical performance of the 3DP-SIHCs device can be ascribed to the porous electrode structure of the 3D printed E-ReSe<sub>2</sub>@INC//AC device that endows sufficient electrode–electrolyte interface contact and accelerates mass transfer (Figure S28, Supporting Information). Notably, E-ReSe<sub>2</sub>@INC//AC 3DP-SIHCs harvest both high gravimetric energy and power densities of 81.4 Wh kg<sup>-1</sup> and 9992.1 W kg<sup>-1</sup>, underscoring the potential of the 3D printing technology (Figure S29, Supporting Information). The 3D-printed SIHCs devices can bridge the gap in the field of the state of the art of batteries and supercapacitors, achieving high energy and power densities simultaneously by integrating the best properties of batteries and supercapacitors (Figure S29, Supporting Information). Figure 5e shows the CV curves of the E-ReSe<sub>2</sub>@INC//AC 3DP-SIHCs device at various scan rates, which still maintains good shape even at a high scan rate of 100 mV s<sup>-1</sup>. The E-ReSe<sub>2</sub>@INC//AC 3DP-SIHCs realizes an areal energy/power density of 0.32 mWh cm<sup>-2</sup>/38.76 mW cm<sup>-2</sup> and volumetric energy density is 3.2 mWh cm<sup>-3</sup>, which is superior compared with most of the capacitor and battery systems fabricated by various printing technologies (Figure 5f; Table S4, Supporting Information).<sup>[35,55–60]</sup> In view of the excellent temperature resistance characteristics of E-ReSe<sub>2</sub>@INC in sodium-ion storage, the 3D-printed E-ReSe<sub>2</sub>@INC//AC SIHCs device also exhibits excellent performance over a wide temperature range (Figure 5g).

### 3. Conclusion

In summary, we propose a topochemistry-driven synthesis strategy for constructing expanded rhenium selenide intercalated by nitrogen-doped carbon hybrid (E-ReSe<sub>2</sub>@INC) with a strongly coupled interface and weak van der Waals forces via a polymer coordination-mediated approach. Subsequently, ex situ XPS and XAS analysis dynamically track the transformation of the coordination structure at the heterointerface from Re–O into Re–C bonds. The strong Re–C bridging bonds at the heterointerfaces enable a controllable interfacial coupling effect and charge transfer channels for improved conductivity and accelerated reaction kinetics. The expanded interlayer-spacing of ReSe<sub>2</sub> layer by INC provides weak van der Waals force, facilitates fast ion diffusion, and ensures high structural stability. As expected, the E-ReSe<sub>2</sub>@INC achieves improved rate capability (252.5 mAh g<sup>-1</sup> at 20 A g<sup>-1</sup>) and long-term cyclability (89.6% over 3500 cycles). Moreover, theoretical simulations confirm the effect of strong bridging bonds-induced interface and weak van der Waals force of the ReSe<sub>2</sub> layer on the improvement for Na<sup>+</sup> bonding energy and ions/electrons diffusion kinetics. Additionally, the as-fabricated 3D-printed sodium-ion hybrid capacitors deliver not only high energy/power density of 81.4 Wh kg<sup>-1</sup>/0.32 mWh cm<sup>-2</sup> and 9992.1 W kg<sup>-1</sup>/38.76 mW cm<sup>-2</sup>, but can be used in a wide temperature range (–20 °C to 50 °C). Therefore, this work offers design principles for building architectures, ranging from microcosmic to macroscopic length scales, for 2D transitional metal dichalcogenides-based electrodes toward hybrid capacitors.

### Supporting Information

Supporting Information is available from the Wiley Online Library or from the author.

### Acknowledgements

The authors are grateful for the financial support from the National Natural Science Foundation of China (22075042), Natural Science Foundation of Shanghai (20ZR1401400, 18ZR1401600), and the Innovation Program of Shanghai Municipal Education Commission (2021-01-07-00-03-E00108). We gratefully acknowledge access to the BL14W1 beamline of Shanghai Synchrotron Radiation Facility (SSRF). J.H. acknowledges financial support from the Research Foundation-Flanders (FWO, Grant No. G983.19N, GOA5817N, and ZW15\_09-G0H6316N), the Flemish government through long-term structural funding Methusalem (CASAS2, Meth/15/04), and the MPI as MPI fellow.

### Conflict of Interest

The authors declare no conflict of interest.

### Data Availability Statement

Research data are not shared.

## Keywords

2D transition-metal selenides, 3D printing, hybrid capacitors, metal-polymer coordination, topochemistry

Received: October 31, 2021

Published online:

- [1] C. Liu, F. Li, L. P. Ma, H. M. Cheng, *Adv. Mater.* **2010**, *22*, E28.
- [2] X. X. Zhang, L. Li, E. S. Fan, Q. Xue, Y. F. Bian, F. Wu, R. J. Chen, *Chem. Rev.* **2020**, *120*, 7020.
- [3] V. Augustyn, P. Simon, B. Dunn, *Energy Environ. Sci.* **2014**, *7*, 1597.
- [4] W. Zhang, Y. Liu, Z. Guo, *Sci. Adv.* **2019**, *5*, eaav7412.
- [5] J. M. Tarascon, M. Armand, *Nature* **2001**, *414*, 359.
- [6] Z. Li, S. Gadipelli, H. Li, C. A. Howard, D. J. L. Brett, P. R. Shearing, Z. Guo, I. P. Parkin, F. Li, *Nat. Energy* **2020**, *5*, 160.
- [7] L. Huang, L. Dai, *Angew. Chem., Int. Ed.* **2017**, *56*, 6381.
- [8] F. Wang, X. Wu, X. Yuan, Z. Liu, Y. Zhang, L. Fu, Y. Zhu, Q. Zhou, Y. Wu, W. Huang, *Chem. Soc. Rev.* **2017**, *46*, 6816.
- [9] Y. Gogotsi, P. Simon, *Science* **2011**, *334*, 917.
- [10] Z. Lei, L. Liu, H. Zhao, F. Liang, S. Chang, L. Li, Y. Zhang, Z. Lin, J. Kroeger, Y. Lei, *Nat. Commun.* **2020**, *11*, 299.
- [11] F. Wang, X. Wang, Z. Chang, X. Wu, X. Liu, L. Fu, Y. Zhu, Y. Wu, W. Huang, *Adv. Mater.* **2015**, *27*, 6962.
- [12] J. Ding, W. Hu, E. Paek, D. Mitlin, *Chem. Rev.* **2018**, *118*, 6457.
- [13] Y. Li, Y. Yang, P. Zhou, T. Gao, Z. Xu, S. Lin, H. Chen, J. Zhou, S. Guo, *Matter* **2018**, *1*, 893.
- [14] H. Liu, X. Liu, S. Wang, H.-K. Liu, L. Li, *Energy Storage Mater.* **2020**, *28*, 122.
- [15] Y. Lu, L. Yu, X. Lou, *Chem* **2018**, *4*, 972.
- [16] Z. Zhu, Y. Tang, Z. Lv, J. Wei, Y. Zhang, R. Wang, W. Zhang, H. Xia, M. Ge, X. Chen, *Angew. Chem., Int. Ed.* **2018**, *57*, 3656.
- [17] C. Yang, J. Feng, F. Lv, J. Zhou, C. Lin, K. Wang, Y. Zhang, Y. Yang, W. Wang, J. Li, S. Guo, *Adv. Mater.* **2018**, *30*, 1800036.
- [18] F. Lai, W. Zong, G. He, Y. Xu, H. Huang, B. Weng, D. Rao, J. A. Martens, J. Hofkens, I. P. Parkin, T. Liu, *Angew. Chem., Int. Ed.* **2020**, *59*, 13320.
- [19] M. Chhowalla, H. S. Shin, G. Eda, L.-J. Li, K. P. Loh, H. Zhang, *Nat. Chem.* **2013**, *5*, 263.
- [20] Q. Zhang, L. Fu, *Chem* **2019**, *5*, 505.
- [21] P. Ge, S. Li, L. Xu, K. Zou, X. Gao, X. Cao, G. Zou, H. Hou, X. Ji, *Adv. Energy Mater.* **2019**, *9*, 1803035.
- [22] L. Li, Y. Zheng, S. L. Zhang, J. P. Yang, Z. P. Shao, Z. P. Guo, *Energy Environ. Sci.* **2018**, *11*, 2310.
- [23] B. Chen, H. Lu, J. Zhou, C. Ye, C. Shi, N. Zhao, S.-Z. Qiao, *Adv. Energy Mater.* **2018**, *8*, 1702909.
- [24] P. Chen, N. Zhang, S. Wang, T. Zhou, Y. Tong, C. Ao, W. Yan, L. Zhang, W. Chu, C. Wu, Y. Xie, *Proc. Natl. Acad. Sci. U.S.A.* **2019**, *116*, 6635.
- [25] H. Jin, S. Xin, C. Chuang, W. Li, H. Wang, J. Zhu, H. Xie, T. Zhang, Y. Wan, Z. Qi, W. Yan, Y.-R. Lu, T.-S. Chan, X. Wu, J. B. H. Goodenough, X. Ji, X. F. Duan, *Science* **2019**, *370*, 192.
- [26] P. Chen, K. Xu, T. Zhou, Y. Tong, J. Wu, H. Cheng, X. Lu, H. Ding, C. Wu, Y. Xie, *Angew. Chem., Int. Ed.* **2016**, *55*, 2488.
- [27] T. Jungst, W. Smolan, K. Schacht, T. Scheibel, J. Groll, *Chem. Rev.* **2016**, *116*, 1496.
- [28] K. Shen, H. Mei, B. Li, J. Ding, S. Yang, *Adv. Energy Mater.* **2018**, *8*, 1701527.
- [29] J. Cai, J. Jin, Z. Fan, C. Li, Z. Shi, J. Sun, Z. Liu, *Adv. Mater.* **2020**, *32*, 2005967.
- [30] H. Yang, W. R. Leow, X. Chen, *Small Methods* **2018**, *2*, 1700259.
- [31] H. Liu, H. Zhang, W. Han, H. Lin, R. Li, J. Zhu, W. Huang, *Adv. Mater.* **2021**, *33*, 2004782.
- [32] B. Yao, S. Chandrasekaran, J. Zhang, W. Xiao, F. Qian, C. Zhu, E. B. Duoss, C. M. Spadaccini, M. A. Worsley, Y. Li, *Joule* **2019**, *3*, 459.
- [33] J. Zhao, H. Lu, Y. Zhang, S. Yu, O. I. Malyi, X. Zhao, L. Wang, H. Wang, J. Peng, X. Li, Y. Zhang, S. Chen, H. Pan, G. Xing, C. Lu, Y. Tang, X. Chen, *Sci. Adv.* **2021**, *7*, eabd6978.
- [34] K. Fu, Y. Wang, C. Yan, Y. Yao, Y. Chen, J. Dai, S. Lacey, Y. Wang, J. Wan, T. Li, Z. Wang, Y. Xu, L. Hu, *Adv. Mater.* **2016**, *28*, 2587.
- [35] Z. Fan, C. Wei, L. Yu, Z. Xia, J. Cai, Z. Tian, G. Zou, S. X. Dou, J. Sun, *ACS Nano* **2020**, *14*, 867.
- [36] Q. Zhang, Y. Zhou, F. Xu, H. Lin, Y. Yan, K. Rui, C. Zhang, Q. Wang, Z. Ma, Y. Zhang, K. Huang, J. Zhu, W. Huang, *Angew. Chem., Int. Ed.* **2018**, *57*, 16436.
- [37] S. Wu, M. Qiu, Z. Tang, J. Liu, B. Guo, *Macromolecules* **2017**, *50*, 3244.
- [38] H. Gao, Z. Zhao, Y. Cai, J. Zhou, W. Hua, L. Chen, L. Wang, J. Zhang, D. Han, M. Liu, L. Jiang, *Nat. Commun.* **2017**, *8*, 15911.
- [39] J. Yan, Y. Huang, Y. Zhang, W. Peng, S. Xia, J. Yu, B. Ding, *Nano Lett.* **2021**, *21*, 2618.
- [40] J. Biener, M. Stadermann, M. Suss, M. A. Worsley, M. M. Biener, K. A. Rose, T. F. Baumann, *Energy Environ. Sci.* **2011**, *4*, 656.
- [41] T.-P. Fellinger, R. J. White, M.-M. Titirici, M. Antonietti, *Adv. Funct. Mater.* **2012**, *22*, 3254.
- [42] Q. Xia, Z. Lin, W. Lai, Y. Wang, C. Ma, Z. Yan, Q. Gu, W. Wei, J.-Z. Wang, Z. Zhang, H. K. Liu, S. X. Dou, S.-L. Chou, *Angew. Chem., Int. Ed.* **2019**, *58*, 14125.
- [43] Z. Lai, A. Chaturvedi, Y. Wang, T. Thu Ha, X. Liu, C. Tan, Z. Luo, B. Chen, Y. Huang, G.-H. Nam, Z. Zhang, Y. Chen, Z. Hu, B. Li, S. Xi, Q. Zhang, Y. Zong, L. Gu, C. Kloc, Y. Du, H. Zhang, *J. Am. Chem. Soc.* **2018**, *140*, 8563.
- [44] H. Funke, A. C. Scheinost, M. Chukalina, *Phys. Rev. B* **2005**, *71*, 094110.
- [45] X. Dong, Z. Guo, Z. Guo, Y. Wang, Y. Xia, *Joule* **2018**, *2*, 902.
- [46] Q. Zhang, Y. Ma, Y. Lu, L. Li, F. Wan, K. Zhang, J. Chen, *Nat. Commun.* **2020**, *11*, 4463.
- [47] J. Qian, F. Wu, Y. S. Ye, M. L. Zhang, Y. X. Huang, Y. Xing, W. Qu, L. Li, R. J. Chen, *Adv. Energy Mater.* **2018**, *8*, 1703159.
- [48] V. Augustyn, J. Come, M. A. Lowe, J. W. Kim, P.-L. Taberna, S. H. Tolbert, H. D. Abruna, P. Simon, B. Dunn, *Nat. Mater.* **2013**, *12*, 518.
- [49] J. O. Hardin, T. J. Ober, A. D. Valentine, J. A. Lewis, *Adv. Mater.* **2015**, *27*, 3279.
- [50] M. A. Skylar-Scott, J. Mueller, C. W. Visser, J. A. Lewis, *Nature* **2019**, *575*, 330.
- [51] Z. Tian, X. Tong, G. Sheng, Y. Shao, L. Yu, V. Tung, J. Sun, R. B. Kaner, Z. Liu, *Nat. Commun.* **2019**, *10*, 4913.
- [52] N. Kurra, Q. Jiang, P. Nayak, H. N. Alshareef, *Nano Today* **2019**, *24*, 81.
- [53] K. Shen, J. Ding, S. Yang, *Adv. Energy Mater.* **2018**, *8*, 1800408.
- [54] W. Zong, N. Chui, Z. Tian, Y. Li, C. Yang, D. Rao, W. Wang, J. Huang, J. Wang, F. Lai, T. Liu, *Adv. Sci.* **2021**, *8*, 2004142.
- [55] T.-S. Wei, B. Y. Ahn, J. Grotto, J. A. Lewis, *Adv. Mater.* **2018**, *30*, 1703027.
- [56] M. Zhu, Z. Wang, H. Li, Y. Xiong, Z. Liu, Z. Tang, Y. Huang, A. L. Rogach, C. Zhi, *Energy Environ. Sci.* **2018**, *11*, 2414.
- [57] T. S. Tran, K. Tripathi, B. N. Kim, I.-K. You, B. J. Park, Y. Han, T. Kim, *Mater. Res. Bull.* **2017**, *96*, 395.
- [58] J. Zhao, Y. Zhang, Y. Huang, J. Xie, X. Zhao, C. Li, J. Qu, Q. Zhang, J. Sun, B. He, Q. Li, C. Lu, X. Xu, W. Lu, L. Li, Y. Yao, *Adv. Sci.* **2018**, *5*, 1801114.
- [59] R. Guo, J. Chen, B. Yang, L. Liu, L. Su, B. Shen, X. Yan, *Adv. Funct. Mater.* **2017**, *27*, 1702394.
- [60] C. Zhang, L. McKeon, M. P. Kremer, S.-H. Park, O. Ronan, A. Seral-Ascaso, S. Barwich, C. O. Coileain, N. McEvoy, H. C. Nerl, B. Anasori, J. N. Coleman, Y. Gogotsi, V. Nicolosi, *Nat. Commun.* **2019**, *10*, 1795.